Fabrication and test of an axial-field HTS rotating machine with integrated magnetic coupling

Bastien Dolisy, Smail Mezani, Thierry Lubin, Jean Lévêque

Fabrication and Test of an Axial-Field HTS Rotating Machine with Integrated Magnetic Coupling

B. Dolisy, S. Mezani, T. Lubin and J. Lévêque

Université de Lorraine, Faculté des Sciences et Technologies, Laboratoire GREEN
BP 70239, 54506, Vandoeuvre-lès-Nancy, France

Abstract

High Temperature Superconducting (HTS) electrical machines have high torque density with a very high efficiency. Torque tubes are usually used to transmit the torque from the cold to the warm environment which results in thermal losses and mechanical problems. To overcome these difficulties, we propose to transmit the torque of the HTS machine through an integrated HTS magnetic coupling. A prototype has been constructed and tested showing the effectiveness of the proposed solution. The machine and the coupling share the same HTS rotor while the torque produced by the machine is transmitted to the load via a permanent magnets rotor. This solution allows the reduction of the thermal losses and a natural protection against overload during fault. The electromagnetic design is carried out using 3D finite elements. The HTS material electrical behavior is described using a power law so it was possible to determine the operating current of the HTS coils of the device. Many test results such as $U(I)$ curves of the HTS coils, static torques, back-EMF and on-load characteristics are presented and checked by the FE computations.

Keywords: HTS rotating machines, magnetic coupling, BSSCO, 3D finite elements, torque transmission, permanent magnets.

1. Introduction

High Temperature Superconducting (HTS) electrical machines provide high torque density with a very high efficiency [1-4]. The compactness of HTS machines makes them very suitable for applications like marine propulsion or electrical wind generation [5-9]. To transmit the torque, “torque tubes” are usually used to mechanically connect the cold HTS rotating inductor to the load located in a warm environment. This critical part has to comply with strong sizing constraints to support the maximal torque during a fault and also to limit the cryogenic losses by thermal conduction [9-13].

In order to suppress the “torque tube”, one can use a magnetic coupling. Indeed, this contactless torque transmission protects the mechanical systems from overloads and jamming of the load. Furthermore, it reduces the thermal conduction when transmitting the torque of HTS machines.

The use of HTS materials in magnetic coupling offers the possibility of transmitting high torque through a large air-gap [14-15] while vibrations due to the space harmonics are practically suppressed.

In this paper, an axial field HTS machine with integrated HTS magnetic coupling is designed, constructed and tested. The motor is composed of a copper armature and a HTS inductor manufactured with BSSCO coils. In the design stage, 3D finite element computations are carried out to obtain the magnetic flux density distribution everywhere in the active parts of the device. Thus, it was possible to determine the operating current of the HTS coils whose electrical behavior is described by the power law.

2. Description of the studied axial field HTS rotating machine

2.1. Active parts

The studied axial field HTS machine shown in Figure 1 is composed of three parts:

- A stator representing the machine armature which consists of a 3-phase 4-pole copper winding fixed on a slotless ferromagnetic yoke. The winding connection diagram is presented in Figure 2, where U, V and W represent the 3 phases.

- An inductor manufactured from four HTS coils placed on each side of a ferromagnetic yoke. The inductor allows the production of a high magnetic field in the both air-gaps (motor and coupler sides). Single and double pancake coils are used in the air-gaps of the magnetic coupling and the motor respectively to adapt their torque maximal values (the torque density of a magnetic coupler is higher than the one of a motor). The HTS coils are supplied with a dc current generator to create alternate poles (north/south) along the azimuthal direction noted θ. To simplify the prototype construction, the eight coils are connected in series and are supplied with the same current noted I_e.

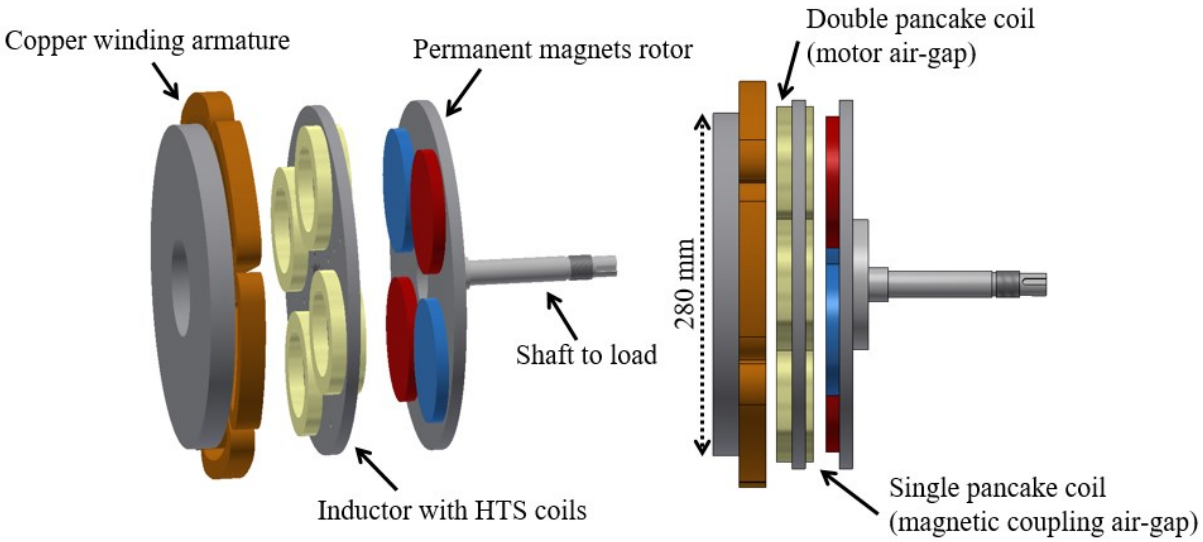

Figure 1 Topology of the studied HTS rotating machine.

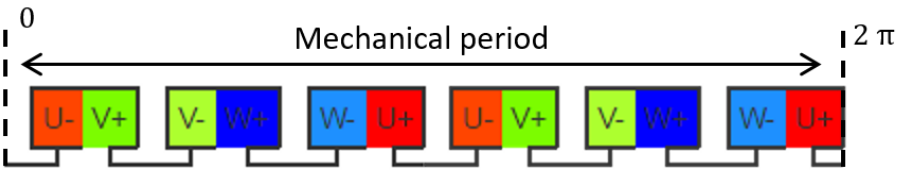

Figure 2 Winding connection diagram of the copper armature.

- A rotor with four permanent magnets (PMs) glued on a ferromagnetic yoke with a north/south alternate polarity (like the HTS coils) and coupled to the load via the mechanical shaft.

In reality, the PMs rotor has been used in a magnetic coupling built in our laboratory and described in an early paper [14]. Hence, all the dimensions of the HTS machine studied here and given in Table 1 have been chosen to comply with the PMs rotor dimensions.

Furthermore, the proposed demonstrator HTS machine with integrated magnetic coupling doesn't fulfil any constraint regarding the torque transmission capabilities. The aim here is to enhance the work described in [14] by constructing and successfully testing a novel HTS machine capable of delivering the torque to its load without any mechanical contact. To our best knowledge, this constitutes a world premiere in the area of HTS electromechanical energy conversion devices.

2.1. Cooling system of the HTS inductor

The machine's rotating inductor is cooled at a temperature of 77K in a liquid nitrogen bath. In order to simplify the construction and for economic usage of the liquid nitrogen, the machine is disposed vertically. A cryostat made of fiberglass (G11 grade) has then been constructed, it is composed of three elements: the base, the tank and the cover (Figure 3). The superconducting coils are connected to a dc supply through two slip-rings and two brushes located on the top of the cryostat cover.

3. 3D Numerical model

A 3D finite element (FE) commercial software (COMSOL Multiphysics®) is used to perform the simulation studies. The ferromagnetic yokes of the prototype are sized to avoid magnetic saturation, so linear FE models are used. Hence, the magnetic field distribution in the machine and the magnetic coupling can be computed separately: motor (armature + HTS inductor) and magnetic coupling (HTS inductor + PMs).

- A magnetic vector potential formulation is adopted to compute the magnetic field distribution in the motor (armature + HTS inductor). Homogeneous current densities are used in the different windings and the relative permeability of the iron yokes is $\mu_r = 1000$. The movement of the HTS rotor is taken into account via a multistatic approach so global quantities like torque and *emf* are computed for different positions of the HTS rotor.

Table 1 Dimensions of the active parts of the HTS machine.

	Description	Units	Value
Main	Mean radius	*mm*	85
	Number of pole pairs	-	2
	Airgap (Coupler / Machine)	*mm*	20 / 5
Copper armature	Number of coils	-	6
	Coils length (axial direction)	*mm*	15
	Coils thickness	*mm*	16
	Coil opening	°	60
	Number of turns per coil	-	250
	Operating current	*A*	7.5
	Iron yoke external radius	*mm*	130
	Iron yoke internal radius	*mm*	40
	Iron yoke thickness	*mm*	20
HTS Inductor	Number of HTS coils (Single / Double)	-	4 / 4
	Coils external radius	*mm*	50
	Coils internal radius	*mm*	35
	Coil thickness per layer	*mm*	5
	Number of turns per layer	-	60
	Length of the HTS tape used per layer	*m*	16
	Operating current (Coupler / Machine)	*A*	57 / 44
	Iron yoke external radius	*mm*	140
	Iron yoke internal radius	*mm*	62.5
	Iron yoke thickness	*mm*	10
PMs rotor	Number of PMs (disc type)	-	4
	Magnet thickness	*mm*	10
	Magnet radius	*mm*	50
	Remanence (sintered NdFeB)	*T*	1.25
	Iron yoke external radius	*mm*	140
	Iron yoke internal radius	*mm*	25
	Iron yoke thickness	*mm*	10

- For the magnetic coupling (HTS inductor + PMs), a magnetic scalar potential formulation is used. In so doing, the pancake coils currents are replaced by an equivalent Coulombian model [17-19] (equivalent magnetization). Again, the movement is taken into account via a multistatic approach so the static torque of the magnetic coupling is computed for different positions.

Figure 5 presents the FE mesh used for the two proposed models (the iron yokes of the PMs rotor and the copper armature are not represented). The mesh is refined until convergent results are obtained.

It has to be noted that the HTS pancake coils are sufficiently meshed in order to have a correct estimation of their magnetic flux density distribution. Indeed, this is a very important issue in order to determine the operating current of the device (see next section).

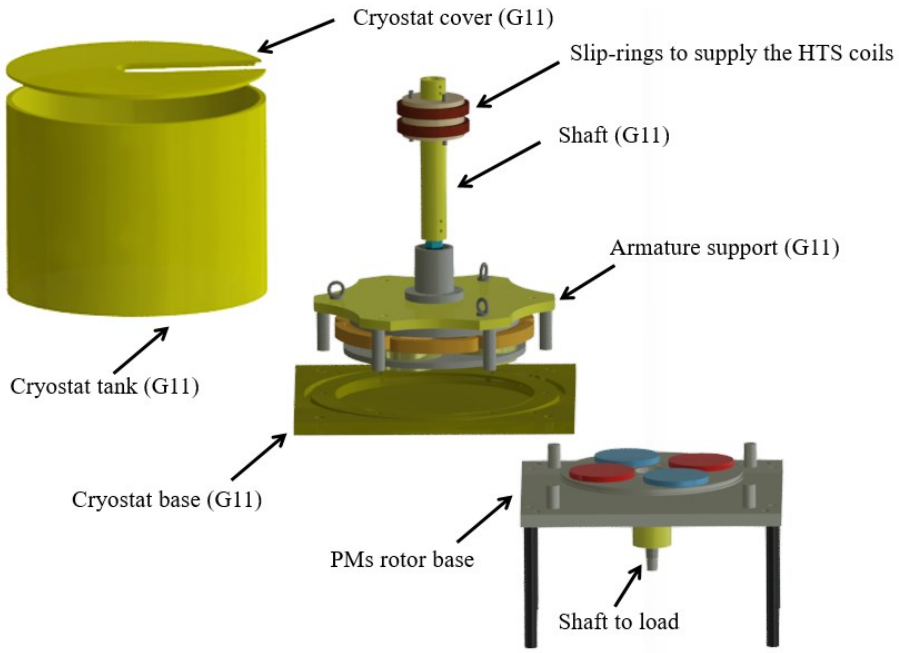

Figure 3 Cooling system of the HTS motor

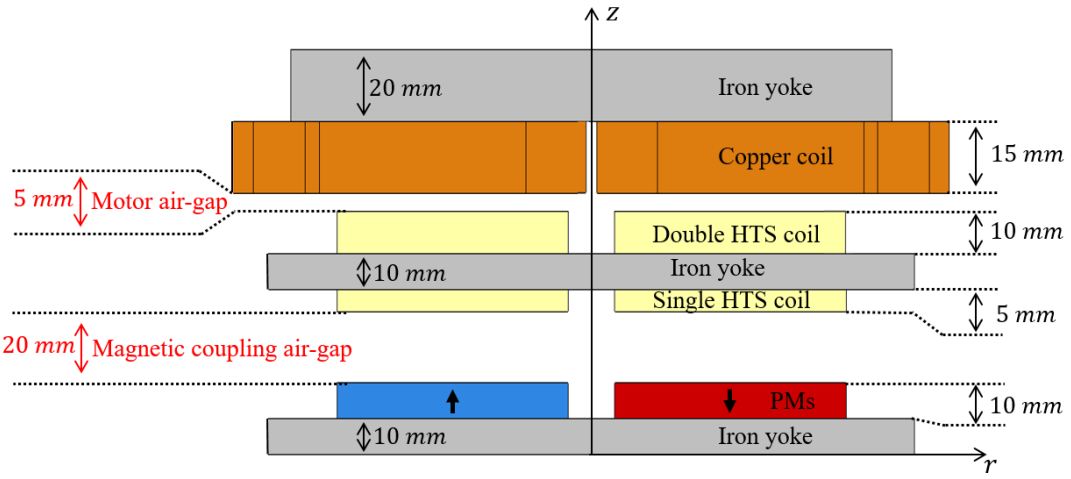

Figure 4 2D axial view of the HTS machine with main dimensions indicated.

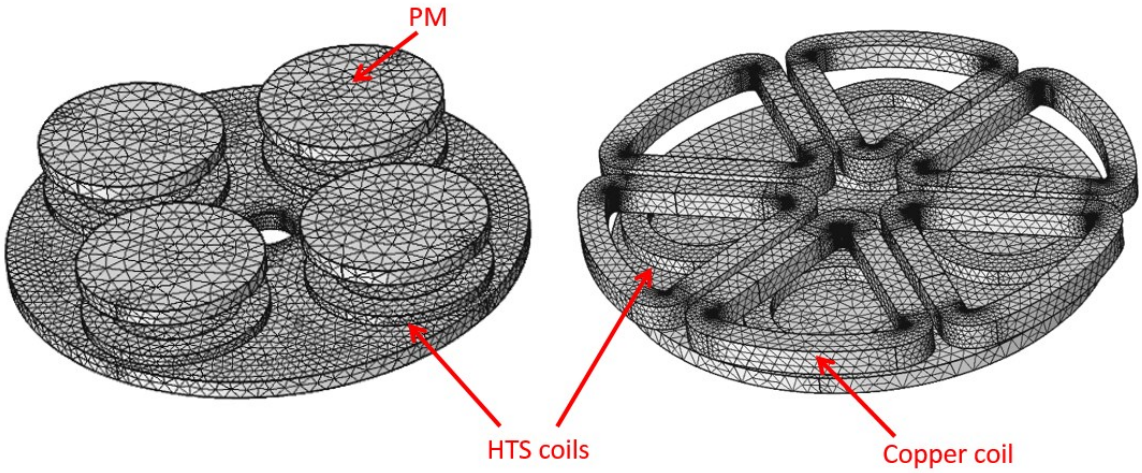

Figure 5 Mesh used in the numerical modeling, left: magnetic coupling, right: motor.

4. Operating current of the HTS coils

In this section, we present a method for the operating current determination of the HTS coils. This theoretical current allows to avoid local transitions (hot spots) and their propagation (quench) in the HTS coils. The model presented below takes into account of the magnetic flux density applied on the coil (computed by FE) and its orientation. The operating current, noted I_M, is defined to respect a maximum electric field criterion in the HTS coil.

4.1. Electrical behavior of the HTS coils

The electric field vs. current density curve $E(J)$ of HTS materials is non-linear and depends on the temperature, the applied magnetic fields and the mechanical stress. Usually, a power law is well suited to model its behavior:

$$\frac{\mathrm{E}}{E_c} = \left(\frac{|J|}{J_c}\right)^{n-1}\left(\frac{J}{J_c}\right) \tag{1}$$

J_c is the critical current density, n is the exponent which defines the transition between the superconducting and the normal states. E_c is the critical electric field which is arbitrary fixed at $E_c = 1\ \mu V/cm$.

At fixed temperature and without mechanical constraints, the operating current only depends on the applied magnetic field and its orientation (anisotropic behavior for BSCCO wires). The magnetic field can have two origins:

- the HTS coil (self-field),
- the magnetic environment surrounding the HTS coil (external field).

The perpendicular magnetic field ($B_\perp$) oriented to the flat side of the HTS tape, has more incidence on the operating current than the parallel magnetic field, noted $B_\parallel$. This behavior is frequently represented by a KIM-ANDERSON like model in which J_c and n depend on the values of ($B_\perp, B_\parallel$), [20-21]:

$$J_c(B_\parallel, B_\perp) = \frac{J_{c0}}{\left(1 + \frac{\sqrt{k^2 B_\parallel^2 + B_\perp^2}}{B_0}\right)^\beta} \tag{2}$$

$$n(B_\parallel, B_\perp) = \frac{n_0}{1 + \frac{\sqrt{k^2 B_\parallel^2 + B_\perp^2}}{B_{n0}}} \tag{3}$$

J_{c0}, B_0, k, β, n_0, B_{n0} are the parameters of relations (2) and (3). They are determined by fitting the experimental $J_c(B_\parallel, B_\perp)$ and $n(B_\parallel, B_\perp)$ curves of an HTS tape sample and are given in Table 2 for a temperature of 77K.

From the FE computation of the magnetic field, one can use (2)-(3) to determine J_c and n and then deduce the electric field E using (1).

Note that under the assumption of a uniform current density in the HTS coils, E is directly proportional to the losses and allows in the present paper to define the operating current. To a certain extent, it is also possible to compute the voltage over a coil's terminals by integration of the electric field as follows:

$$U = \frac{N_{turn}}{S_{coil}} \iiint_{V_{coil}} E(x,y,z)\,dx\,dy\,dz \tag{4}$$

where N_{turn} is the number of turns of the HTS pancake coil, V_{coil} its volume and S_{coil} its cross section area.

4.2. Maximal electric field criterion and results

The operating current I_M is set to limit the value of the electric field (E) by defining a criterion which depends on the cryogenic capacity to extract the Joule losses (cryogenic power, cooling technology…).

In this study, the authorized maximal electric field is taken equal to the critical electric field:

$$\max(E) = E_c \tag{5}$$

Figure 6 presents the iterative method for I_M computation. Each calculation step corresponds to a FE result, computed for a given inductor current. As long as the criterion is respected, the current value into the HTS coils is incremented.

Table 2 HTS tape parameters at 77K

	Parameter	Units	Value
J_c	J_{c0}	A/mm^2	184
	B_0	T	0.175
	β	-	1.765
	k_a	-	0.1
n	n_0	-	23
	B_{n0}	T	0.061
	k_a	-	0.1

This method allows to take into account the non-linearity of the materials, the external magnetic sources and the relative position between the different rotors (internal angle).

Figure 7 shows the maximal electric field in the HTS coils versus the current for the magnetic coupling (left) and the motor (right) respectively. The operating current I_M is reached when $E/E_c=1$. The calculations have been carried out for the no-load and maximum torque positions. The currents in the 3 phases of the stator winding are $I_1 = I$, $I_2 = -I/2$ and $I_3 = -I/2$, with $I = 7{,}5A$.

The operating current of the HTS inductor is about $57\ A$ for the magnetic coupling and $44\ A$ for the motor.

Figure 8 gives more details on the internal angle effects. In the case of the magnetic coupling (left), we note a difference of 12% between the higher and lower values of I_M.

This shows the influence of the external field due to the magnets position. Thus, it is important to compute the operating current in the most critical position (here at the maximal torque).

For the motor, the inductor position has only a little influence on I_M. This is because the magnitude of magnetic flux density created by the stator is much lower than that of the HTS coils.

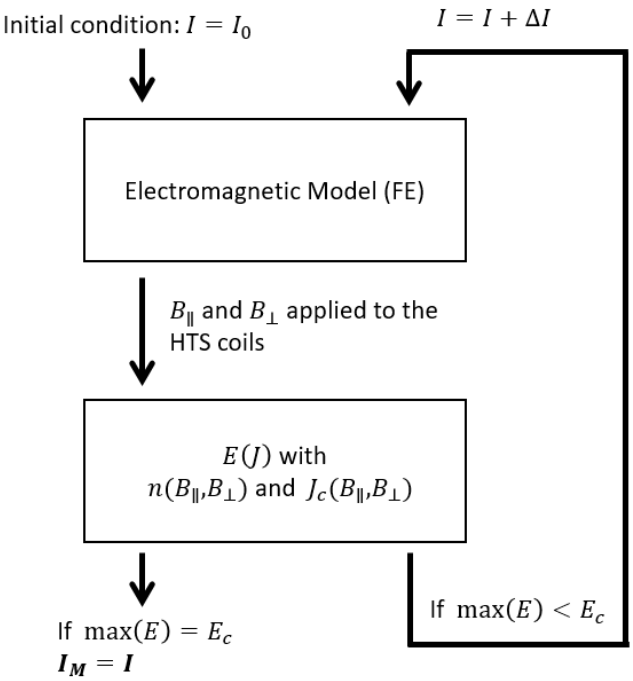

Figure 6 Method for the operating current determination of the HTS coils.

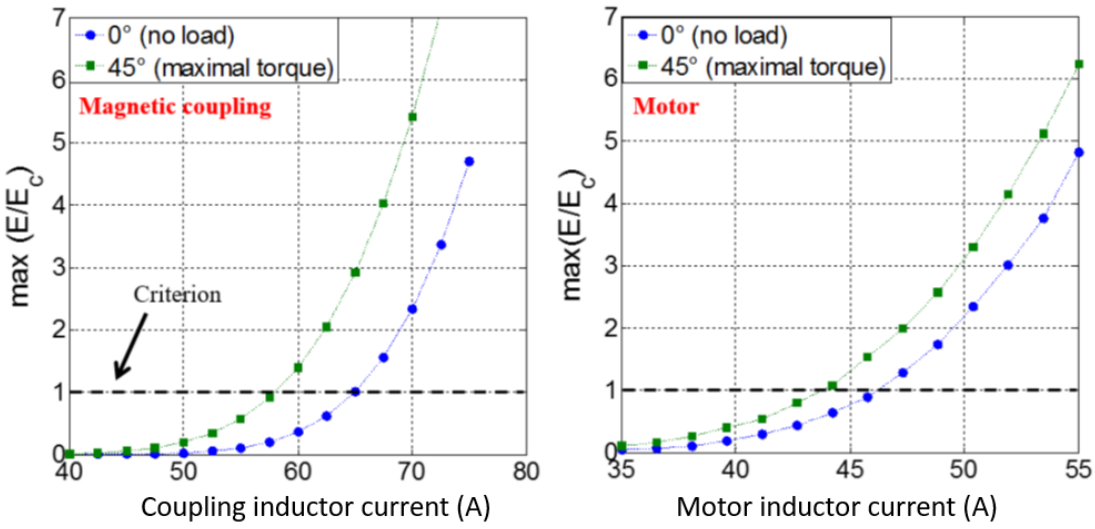

Figure 7 max(E/E$_c$) in the HTS coils for no-load and maximal torque positions left: magnetic coupling, right: motor (calculated data).

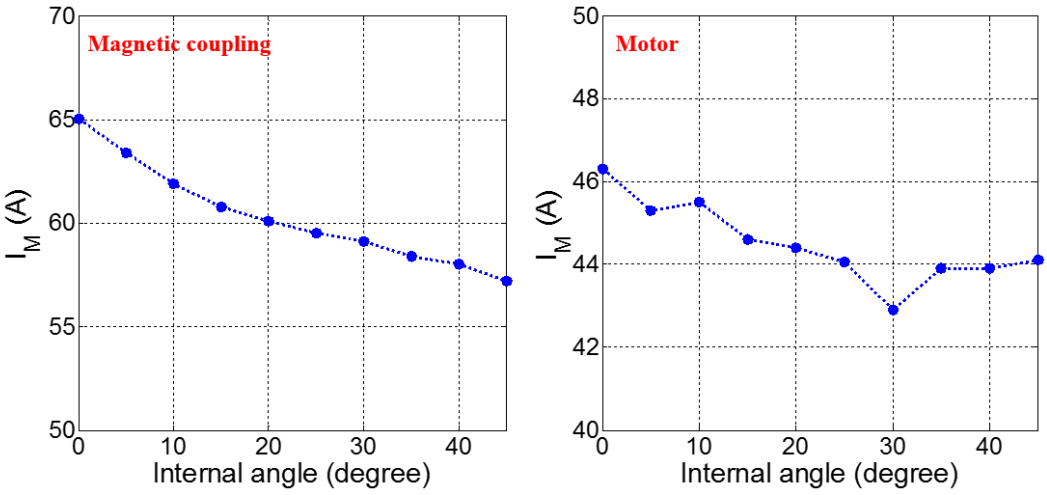

Figure 8 I_M versus the internal angle, left: magnetic coupling, right: motor (calculated data).

5. Manufacturing of the HTS rotating machine

5.1. The HTS inductor

Two kind of HTS coils have been manufactured:

- four double pancake coils for the machine side
- four single pancake coils for the magnetic coupling side

The coils are supplied with a dc current to create 4 poles. They are disposed in the air-gaps of the motor and the magnetic coupling respectively. The HTS coils consist of insulated DI-BSCCO/Ag (Bismuth Strontium Calcium Copper Oxide) multi-filamentary tape commercialized by Sumitomo Electric (Type H_i) [16]. The dimensions of the tape are $0.25\,mm$ thickness and $4.4\,mm$ width (insulation included), their critical bending diameter is $70\,mm$. Its critical current is $I_c = 190\,A$ at $77\,K$ under a critical electric field $E_c = 1\ \mu V/cm$.

The manufactured coils are shown in Figure 9 and their dimension are presented in Table 1 above. During the winding process, the tape is impregnated with epoxy resin (Araldite AY 103-1) for mechanical reinforcement. In order to perform electric tests (4-wire method), each coil is equipped with two current leads and two voltage taps. Thus, the voltage vs. current $U(I)$ curve of individual coil is measured at $77K$ with no-external magnetic field. These curves have been also computed by finite elements using (4). The similarity of the measured curves shown Figure 10 demonstrates the integrity of the HTS coils. Furthermore, the computed curves are also consistent with the measured ones.

After the previous tests, the eight HTS coils have been fixed on a solid ferromagnetic yoke (4 coils per face), Figure 11. They are electrically connected in series to produce a 4-pole magnetic field in the air-gaps of the machine and the magnetic coupling sides.

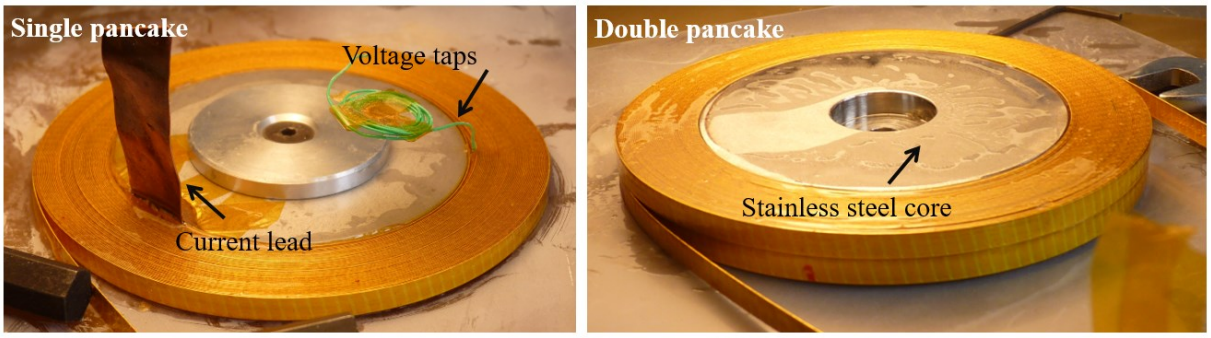

Figure 9 Photographs of the manufactured HTS coils, left: single pancake and right: double pancake.

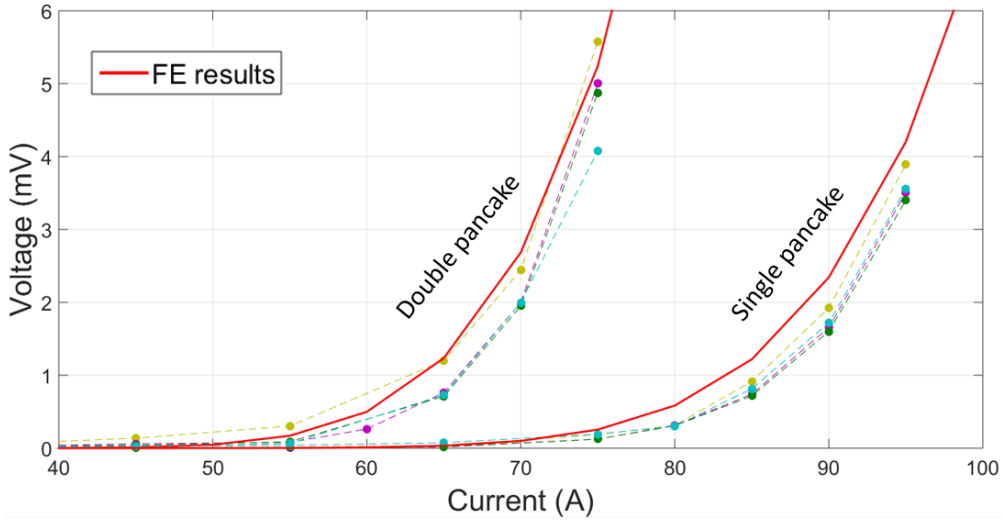

Figure 10 Measured and calculated $U(I)$ curves at the terminals of each coil at 77K (zero external magnetic field).

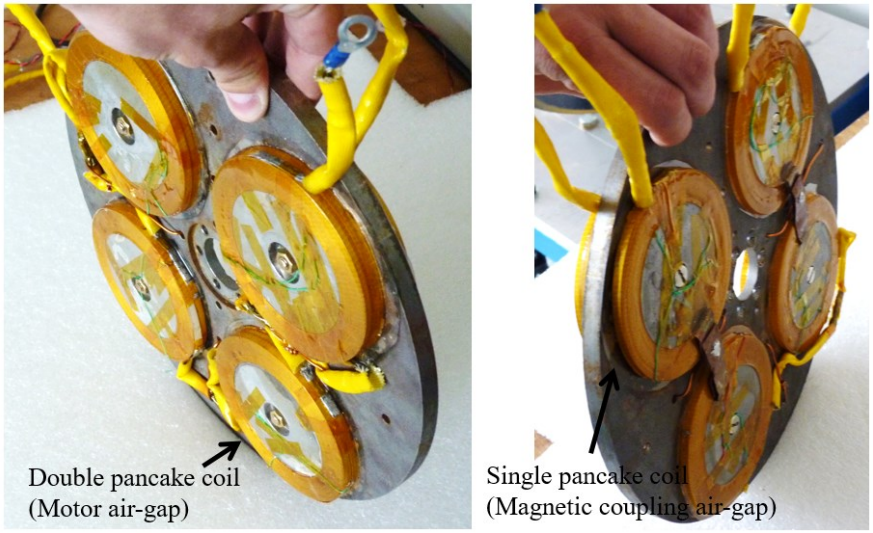

Figure 11 Photographs of the HTS inductor, left: motor side and right: magnetic coupling side.

5.2. Copper armature

The copper armature (stator) shown in

Figure 12 consists of 6 identical coils with 250 turns each ($0{,}75\ mm^2$ of active section wire). After being wound, the coils are fixed on the ferromagnetic yoke and impregnated with epoxy resin (Araldite AY 103-1). Since the armature winding is supplied with ac currents, it has to be laminated to reduce the iron losses. Thus, the yoke is made from rolled FeSi laminations ($0.3\ mm$ thickness).

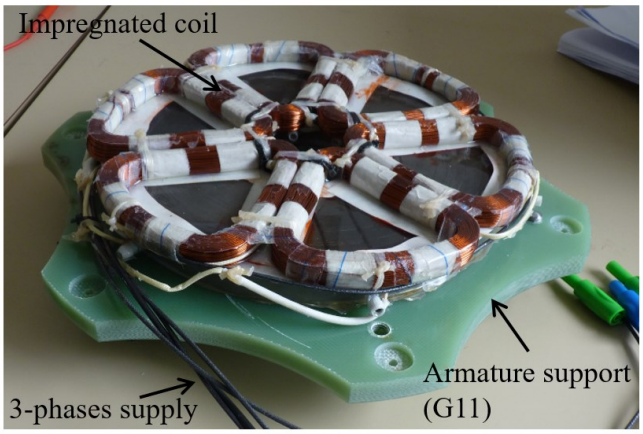

Figure 12 Photographs of the copper armature.

5.3. PMs rotor

As mentioned above, the PMs rotor comes from an earlier magnetic coupling prototype constructed in our Lab [14]. It consists of four identical disc NdFeB magnets, with $100\ mm$ diameter and $10\ mm$ thickness, glued on a solid ferromagnetic yoke. The remanent flux density of the magnets is equal to $1.25\ T$.

5.4. Test bench

A separately excited DC machine is mechanically coupled to the HTS machine through the PMs rotor. Its rated characteristics are: $4{,}1\ kW$ $840\ rpm$ $460\ V$ $14\ A$. Two incremental encoders are connected to the HTS inductor and to the DC motor respectively. Finally, the static torque (motor and magnetic coupling) are measured using a torque sensor placed between the incremental encoder (inductor side) and the HTS inductor. This sensor measures torques up to $30\ Nm$ with a precision of $0{,}77\%$ of the full range (max error of 0.23 Nm).

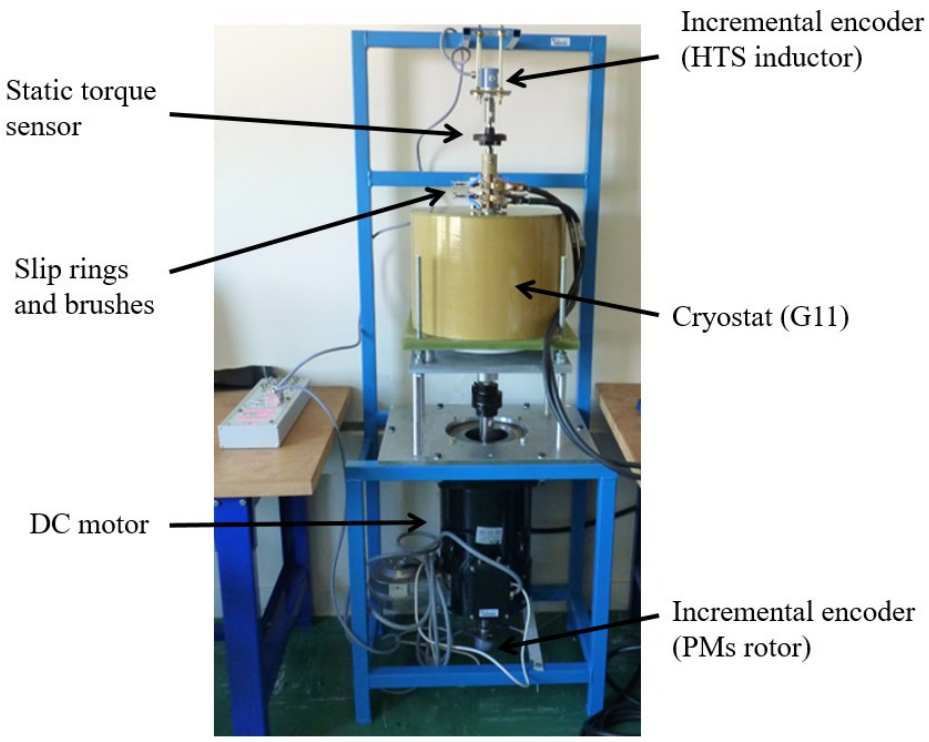

Figure 13 Photograph of the test bench.

6. Prototype tests and results

In this section, we present the principal tests carried out on the constructed and assembled HTS machine.

6.1. HTS coils characterization

Figure 14 shows the measured and computed $U(I)$ curves of the HTS coils located in the air-gaps of the magnetic coupling and the motor respectively. The tests have been carried out for the no-load position and with the current armature defined earlier ($I_1 = I$, $I_2 = -I/2$ and $I_3 = -I/2$ with $I = 7{,}5\ A$). The measured electric characteristics of the HTS coils are very similar which shows their integrity and the good manufacturing process. The FE computed U(I) curves using (4) are also consistent with the measured ones.

For the double-pancake coils (machine side), the length of the HTS tape is 32 m (see Table 1), which results in a critical voltage of 3.2 mV (1 µV/cm critical electric field). Hence, the corresponding critical current is about 60A. The computed value of the operating current using the max(E) criteria at no load (Figure 8) is about 46 A, which is 23% lower than the critical current. This clearly shows that it is crucial to consider local criteria in defining an operating current rather than a global one.

Nevertheless, if only measured U(I) curves are available, it is possible to define an operating current equals to a critical current obtained for a lower critical electric field [14], [22]. By considering a critical electric field of 0.1 µV/cm [22]. the operating current deduced from figure 14 is about 47A, which is very close to the computed operating current of 46 A.

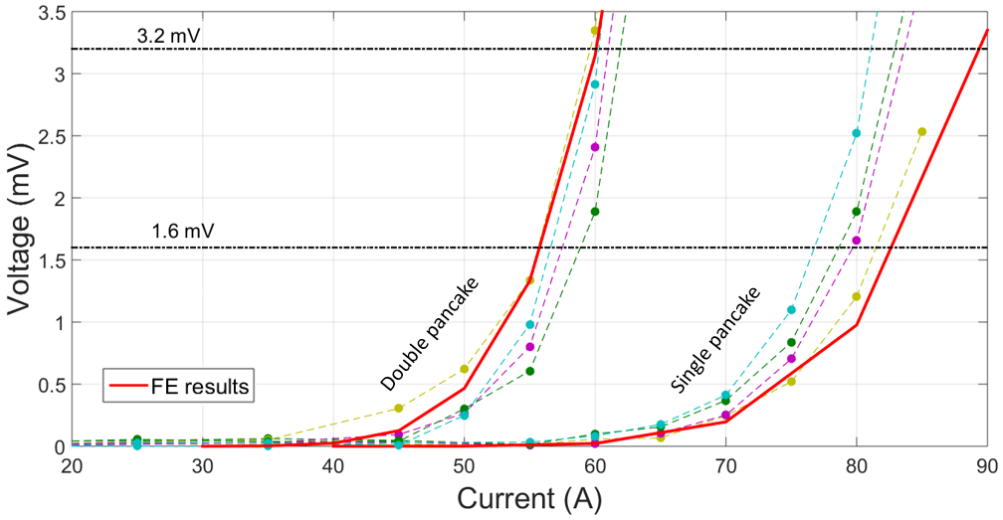

Figure 14 Measured and computed $U(I)$ curves of the HTS coils located in the magnetic coupling (single pancake) and motor (double pancake) air-gaps at no load

6.2. Static torque

Figure 15 presents the static torque measurement protocol. The torque is imposed through a lever arm (by applying a force) and is measured with a torque sensor.

Figure 16 compares the experimental results with the FE ones for inductor currents $I_e = 25\ A$ and $I_e = 45\ A$. The copper armature is supplied with 3-phase currents as done previously ($I_1 = I$, $I_2 = -I/2$ and $I_3 = -I/2$ with $I = 7{,}5\ A$).

For $I_e = 25\ A$, the 3D FE predictions give pull-out torques of about 7 Nm (motor) and 15 Nm (magnetic coupling) while the measurements give almost the same values. For the other load angle values, the relative difference between the tests and the simulation results doesn't exceed 15%.

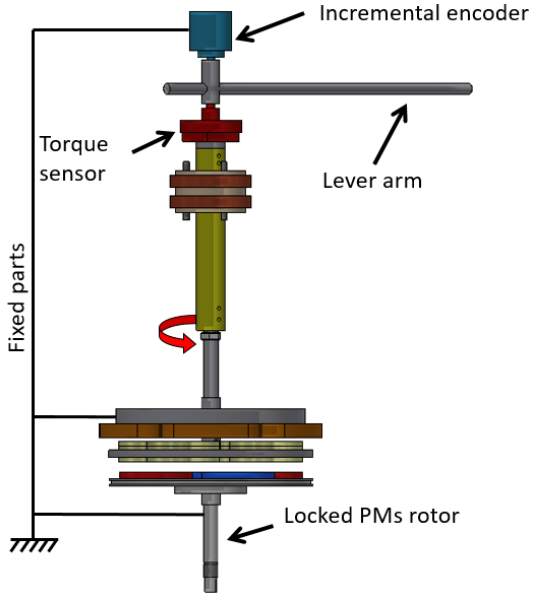

Figure 15 Measurement protocol of the static torque.

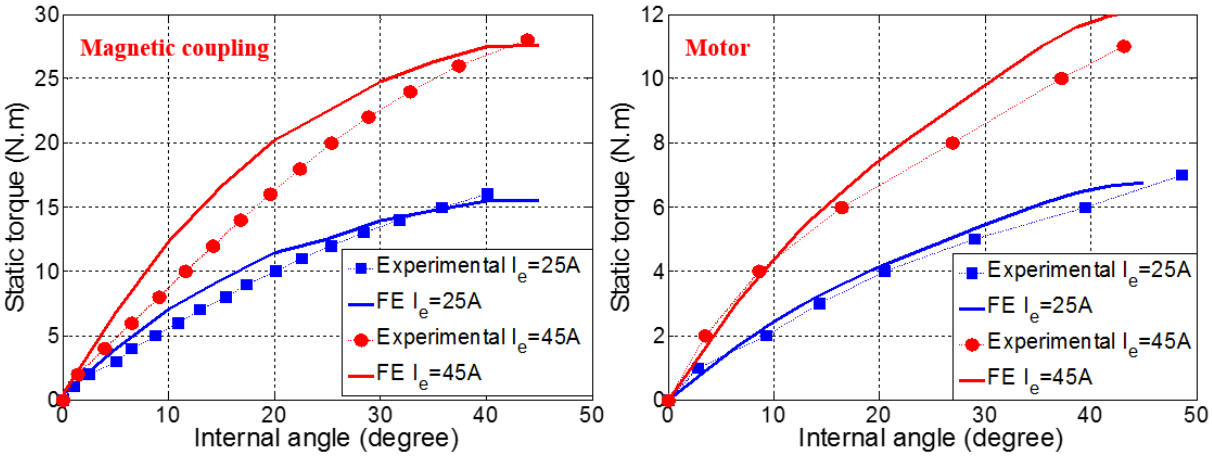

Figure 16 Static torque measured for inductor currents $I_e = 25\ A$ and $45\ A$, left: magnetic coupling, right: motor.

For $I_e = 45\ A$, the relative difference between the tests and the simulation results doesn't exceed 20%. However, the predicted and the measured pull-out torques are very close for both the motor and the magnetic coupling.

6.3. No-load and short-circuit tests

Figure 17 shows the measured and calculated per phase back-EMF waveforms and their harmonic spectra for $I_e = 50\ A$ at $500\ rpm$. The measured and computed curves are in good accordance except for the computed 3rd harmonic which is underestimated compared to the tests. It can be observed that the 3rd harmonic represents almost 13% of the fundamental back-EMF. This is due to the very simple armature winding which has not been optimized to reduce space harmonics.

Nevertheless, apart from the case when we need to use the neutral, the armature of 3-phase machines is supplied by 3-wires. Hence, the line voltage doesn't exhibit a 3rd harmonic and its multiples.

Figure 18 presents the no-load back-EMF and the short-circuit current vs. inductor current for a rotation speed of $250\ rpm$. It can be seen that the $E(I_e)$ curve is almost linear.

From these two tests, one can deduce the synchronous reactance of the machine noted X_s. The presented results lead to $X_s = 1.98\ \Omega$ at 250 rpm, which corresponds to a synchronous inductance $L_s = 37.8\ mH$. We have also measured the armature per phase resistance which is equal to $R_s = 0.82\ \Omega$. Knowing R_s and L_s, it is possible to determine the steady state machine performances using the phasor diagram of smooth air-gap synchronous machines.

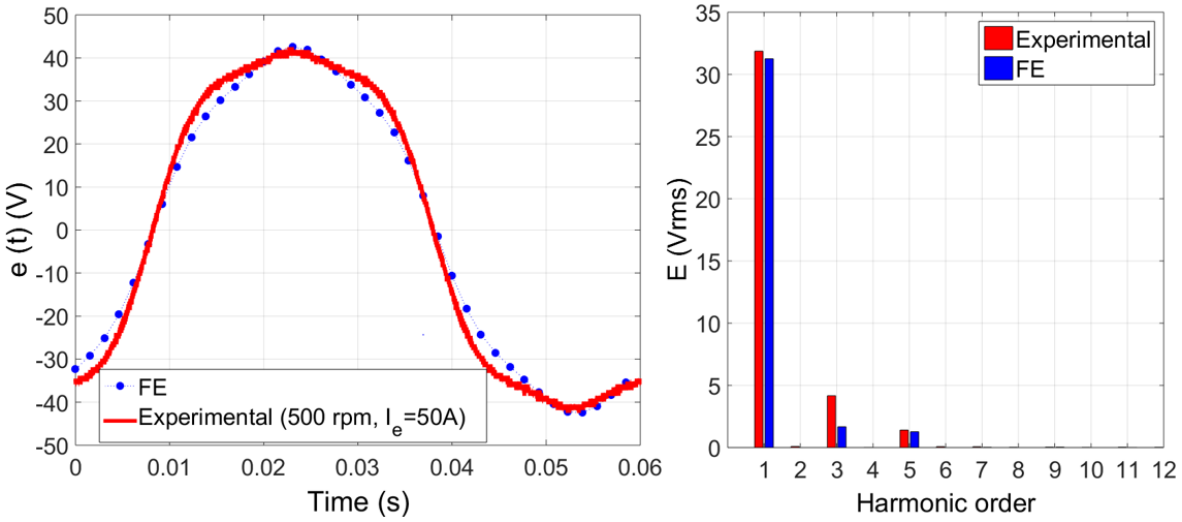

Figure 17 Back-EMF for $I_e = 50\ A$ at $500\ rpm$, left: back-EMF waveform, right: harmonic spectra.

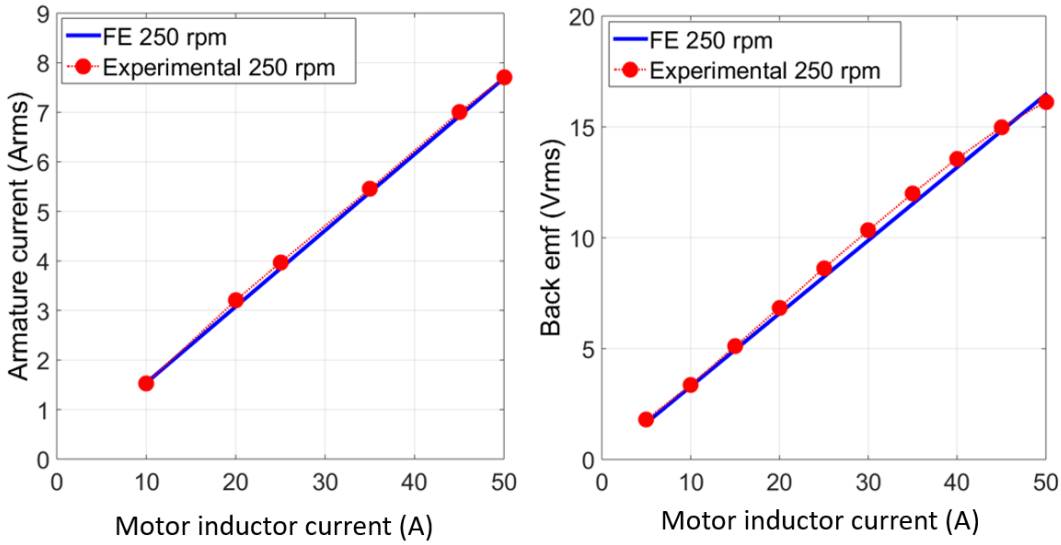

Figure 18 Reduced power tests and simulations at $250\ rpm$
left: short-circuit current $I_{armature}$ vs I_e, right: no-load back-EMF vs I_e.

6.4. Load test in generator mode

We have carried out load tests of the HTS machine in generator mode. The machine is driven by the DC motor which imposes the speed. The copper armature is connected to a 3-phase balanced resistive load. For rotating speeds of $250\ rpm$ and $500\ rpm$, Figure 19 presents the voltage vs armature current curves obtained by varying the load resistance. It can be seen that the agreement between the experimental and the computed results is very good. This result show the good operation of the superconducting motor with the magnetic coupling.

At 500 rpm and with an electromagnetic torque of 10 Nm ($I_e = 50\ A$), we reach a power of 500 Watts. Obviously, this prototype cooled at 77K has limited capabilities in terms of power and torque densities. But the aim here is to demonstrate that the concept of HTS machine with integrated magnetic coupling works properly.

We are currently working on a more sophisticated cooling system for our demonstrator to achieve high power/torque densities. Using cryocoolers, we can operate at 20–30 K to increase the operating current to at least 200 A. Preliminary calculations have shown that the HTS inductor of our prototype can produce a peak flux density up to 1.8 T in the air gap. This represents twice the usual value of air gap flux densities in conventional PM machines.

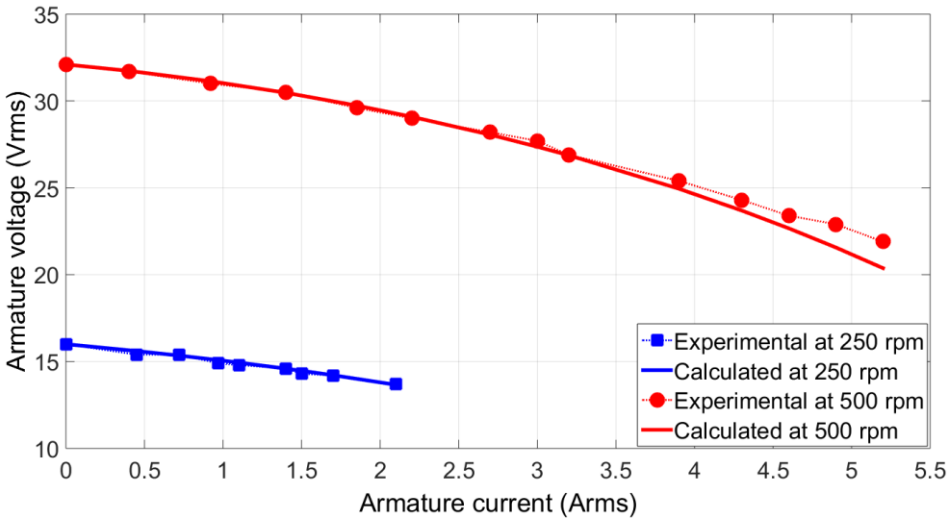

Figure 19 Armature voltage-current U(I) curves in generator mode with a resistive load at $250\ and\ 500\ rpm$ *(*$I_e = 50\ A$*).*

Conclusion

A novel HTS axial field machine with an integrated HTS magnetic coupling has been designed, constructed and tested. Many fabrication details have been provided and the testing results successfully demonstrated the good operation of the proposed solution.

Further studies are ongoing in order to operate at 20–30 K which are the usual working temperatures for achieving high power/torque densities.

Acknowledgement

The authors would like to thank the DGA (Direction Générale de l'Armement) for funding this work.

References

[1] Sugimoto, H., Morishita, T., Tsuda, T., Takeda, T., Togawa, H., Oota, T., ... & Yoshida, S. (2008). Development and test of an axial flux type PM synchronous motor with liquid nitrogen cooled HTS armature windings. In Journal of Physics: Conference Series (Vol. 97, No. 1, p. 012203). IOP Publishing.

[3] Dezhin, D., Ilyasov, R., Kozub, S., Kovalev, K., & Verzhbitsky, L. (2014). Synchronous motor with HTS-2G wires. In Journal of Physics: Conference Series (Vol. 507, No. 3, p. 032011). IOP Publishing.

[3] Qu, T., Song, P., Yu, X., Gu, C., Li, L., Li, X., ... & Han, Z. (2014). Development and testing of a 2.5 kW synchronous generator with a high temperature superconducting stator and permanent magnet rotor. Superconductor Science and Technology, 27(4), 044026.

[4] Snitchler, G., Gamble, B., & Kalsi, S. S. (2005). The performance of a 5 MW high temperature superconductor ship propulsion motor. Applied Superconductivity, IEEE Transactions on, 15(2), 2206-2209.

[5] Moon, H., Kim, Y. C., Park, H. J., Park, M., & Yu, I. K. (2016). Development of a MW-Class 2G HTS Ship Propulsion Motor. IEEE Transactions on Applied Superconductivity, 26(4), 1-5.

[6] Umemoto, K., Aizawa, K., Yokoyama, M., Yoshikawa, K., Kimura, Y., Izumi, M., ... & Gocho, Y. (2010). Development of 1 MW-class HTS motor for podded ship propulsion system. In Journal of Physics: Conference Series (Vol. 234, No. 3, p. 032060). IOP Publishing.

[7] Yang, Y., Duan, S., Ren, Y., Jiang, Y., Feng, L., Zhang, X., ... & Zhao, Y. (2016). Design and Development of a Cryogen-Free Superconducting Prototype Generator With YBCO Field Windings. IEEE Transactions on Applied Superconductivity, 26(4), 1-5.

[8] Gamble, B., Snitchler, G., & MacDonald, T. (2011). Full power test of a 36.5 MW HTS propulsion motor. Applied Superconductivity, IEEE Transactions on,21(3), 1083-1088.

[9] Snitchler, G., Gamble, B., King, C., & Winn, P. (2011). 10 MW class superconductor wind turbine generators. Applied Superconductivity, IEEE Transactions on, 21(3), 1089-1092.

[10] Fang, H., Qu, R., Wang, J., Zhu, Z., & Chen, H. (2015). Design of a Novel Torque Tube for a Direct-Drive Superconducting Wind Generator. IEEE Transactions on Applied Superconductivity, 25(3), 1-4.

[11] Qu, T., Wu, Q., Feng, F., Song, P., Hong, Z., Sun, R., Han, Z. (2016). Design and Test of a Novel Thermal Insulated Torque Coupling for a 15-kW Fully HTS Synchronous Generator. IEEE Transactions on Applied Superconductivity, 26(3), 1-5.

[12] Al-Mosawi, Maitham K., BEDUZ, C., YANG, Y. Construction of a 100 kVA high temperature superconducting synchronous generator. Applied Superconductivity, IEEE Transactions on, 2005, vol. 15, no 2, p. 2182-2185.

[13] Kummeth, P., Frank, M., Nick, W. et al. Development of synchronous machines with HTS rotor. Physica C: Superconductivity, 2005, vol. 426, p. 1358-1364.

[14] Belguerras, L., Mezani, S., Lubin, T., Lévêque, J., & Rezzoug, A. (2015). High temperature superconducting axial field magnetic coupler: realization and test. Superconductor Science and Technology, 28(9), 095003.

[15] Ma, K. B., McMichael, C. K., Lamb, M. A., & Chu, W. K. (1993). Application of high temperature superconductors on levitation bearings, torque transmissions and vibration dampers. Applied Superconductivity, IEEE Transactions on, 3(1), 388-391.

[16] Sumitomo Electric, HTS tape supplier, website: http://global-sei.com/super/hts_e/.

[17] Charpentier, J. F. and Lemarquand, G. Study of permanent-magnet couplings with progressive magnetization using an analytical formulation. Magnetics, IEEE Transactions on, 1999, vol. 35, no 5, p. 4206-4217.

[18] Rakotoarison, Harijaona Lalao, Yonnet, Jean-Paul, and DELINCHANT, Benoît. Using coulombian approach for modeling scalar potential and magnetic field of a permanent magnet with radial polarization. In : IEEE Transactions on Magnetics. 2007. p. 1261-126.

[19] Bruzzone. P 2004 Physica C Superconductivity 401 7-14.

[20] Zermeño, V. M., & Grilli, F. (2014). 3D modeling and simulation of 2G HTS stacks and coils. Superconductor Science and Technology, 27(4), 044025.

[21] Kim, Y. B., Hempstead, C. F., and Strnad, A. R. Critical persistent currents in hard superconductors. Phys. Rev. Letters, 1962, vol. 9.

[22] Pitel J. Differences between two definitions of the critical current of HTS coils. Supercond. Sci. Technol. 2013, 26 125002.